



Finite element analysis of mechanical behavior of electrical wire harnesses: High fidelity and reduced-order models

Ehsan Taghipour^a, Sai Siddhartha Vemula^a, Kushal Gargesh^c, Leon M. Headings^a, Marcelo J. Dapino^a, Soheil Soghrati^{a,b,*}

^a Department of Mechanical and Aerospace Engineering, The Ohio State University, Columbus, OH, USA

^b Department of Materials Science and Engineering, The Ohio State University, Columbus, OH, USA

^c Honda R&D Americas, Raymond, OH, USA

ARTICLE INFO

Keywords:

Composite wire harness
Finite element method
Bending
Reduced-order model
Wire harness branching

ABSTRACT

High-fidelity and reduced-order finite element (FE) models are introduced to simulate and characterize the bending behavior of flexible electrical wire harnesses undergoing large deflections. A composite wire harness consists of a bundle of wires, put together using layers of tape and/or a protective tube, which could be subdivided into smaller branches. In this work, elastoplastic constitutive models are adopted for wire harness components (wires, tape, and tube) and calibrated by matching their simulated and experimental force-displacement responses. Customized three-point bending tests are carried out on composite wire bundles (CWBs) and resulting data are utilized to calibrate friction coefficients between different components, as well as cohesive contact and damage parameters along taped surfaces in the high-fidelity FE model. After the validation of this model, we show that it can be used as a reliable surrogate to laborious mechanical testing for characterizing the bending response of CWBs. Resulting effective properties are then incorporated in a reduced-order FE model relying on beam elements, which can achieve a similar level of accuracy while reducing the computational cost > 99.5%. Both FE models are also employed to study the behavior of branching wire harnesses, showing that a viscoelastic material model is needed to properly characterize the stiffness of the branch break-out joint.

1. Introduction

Predicting the deformation response of flexible electrical wire harnesses during the assembly process is a critical design requirement in the automotive industry. Numerical and analytical modeling of wire harnesses in digital manufacturing software packages aim to achieve this goal by minimizing the computational cost (near real-time simulations) while maintaining an acceptable accuracy. However, building a model that could fulfill this objective is a challenging task due to the highly nonlinear geometrical and material behaviors of flexible wire harnesses, as well as the uncertainty associated with their dimensions and loading history (e.g., residual stresses). Further, the design and execution of experimental testings needed for the calibration/validation of such models are laborious and could be equally challenging due to the soft, intricate internal architecture of harnesses composed of various types/sizes of wires, tapes, and protective tubes, which could also involve multiple branches. Among previous research efforts dedicated to modeling wire harnesses and similar flexible structures we can mention analytical models [1–6], finite element (FE) analyses [7–13], and experimental works [14–19]. Combined analytical-computational approaches

have also been implemented to analyze the axial, torsional, and flexural behaviors of composite wires and conductors [20–22].

The design of wire harnesses is also addressed in a number of previous studies, which involves an iterative, time-consuming process. Among these works we can mention attempts at optimizing the geometry, mechanical integrity, and electrical connectivity [23,24], as well as minimizing the production time, cost, and overall weight of wire harnesses [23–26]. The *Virtual Reality* (VR) environment can also be utilized to address different design stages more efficiently [27]. Among other relevant studies we can mention techniques developed for the design of the break-out joint while mounting wire harnesses on vehicle bodies [28–32]. These techniques aim to determine connecting arrangements of wire and wire bundle branches to reduce the weight, number of components, and required space without failure at connectors while simplifying the assembly process. However, nearly all existing models used in digital manufacturing and VR environments cannot accurately predict the deformed shape and mechanical behavior of complex wire harnesses, which often leads to non-optimal design configurations. The main reason for this lack of predictive capability is the use of either inappropriate material and interaction properties or unrealistic models

* Corresponding author.

E-mail address: soghrati.1@osu.edu (S. Soghrati).

<https://doi.org/10.1016/j.ijmecsci.2019.105188>

Received 24 March 2019; Received in revised form 28 August 2019; Accepted 23 September 2019

Available online 25 September 2019

0020-7403/© 2019 Elsevier Ltd. All rights reserved.

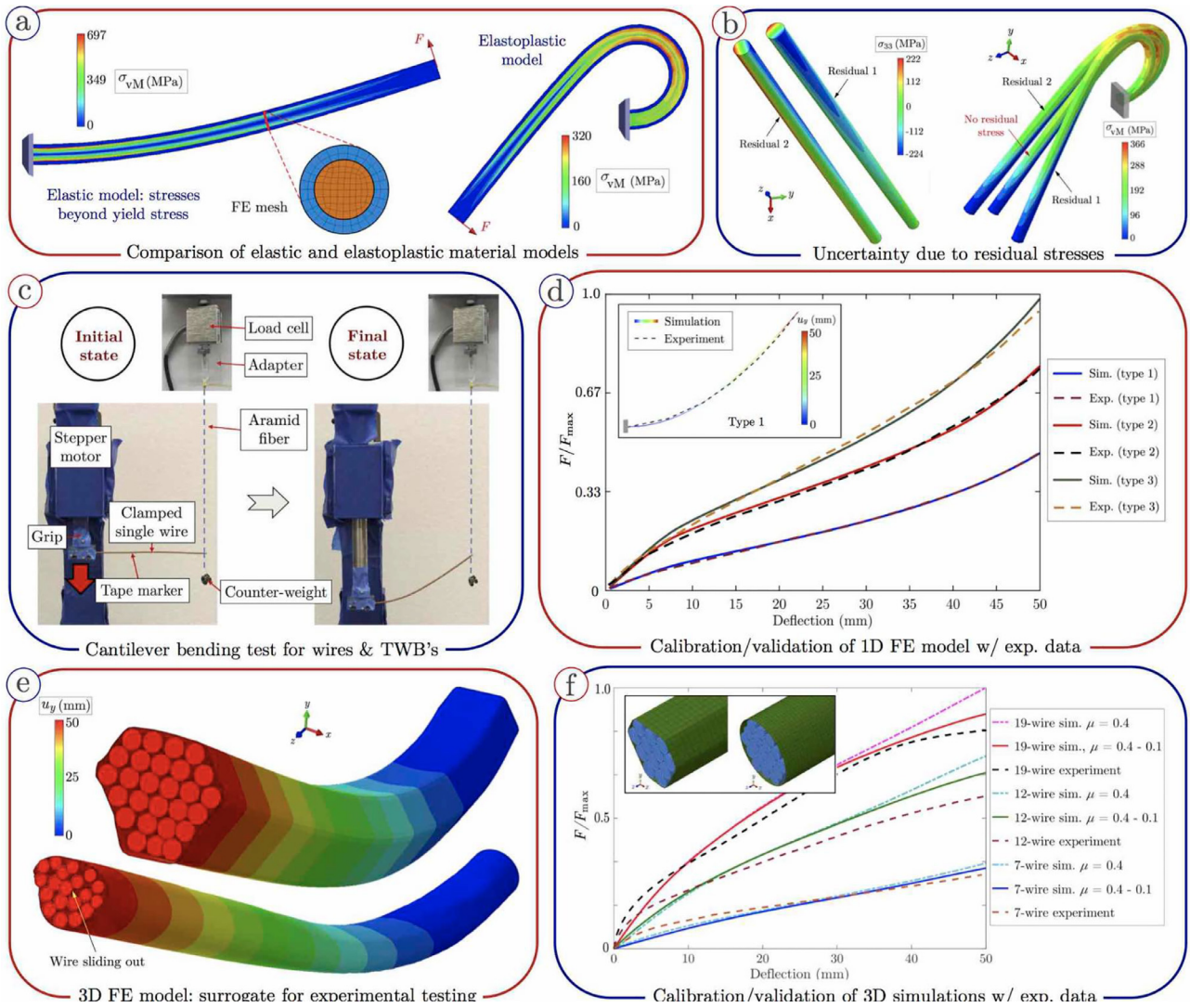


Fig. 1. Graphical summary of [33], which serves as the basis of the study presented in the current manuscript.

(e.g., overlooking nonlinearity) for harness components during the simulation.

The current manuscript aims to expand the synergistic experimental-numerical framework presented in [33] for analyzing the deformation response of taped wire bundles (TWBs) to enable evaluating the behavior of composite wire bundles (CWBs) and branching wires harnesses. A graphical summary of [33] is presented in Fig. 1, where reduced-order (1D) and high-fidelity (3D) FE models are employed to simulate the bending response of single wires and TWBs. As shown in Fig. 1a, one of the key outcomes of the study was that taking into account the elastoplastic behavior of wires is of crucial importance for the accurate prediction of mechanical behavior subject to bending loads. We also studied the uncertainty associated with the presence of residual stresses on the behavior of wires (cf. Fig. 1b). Customized cantilever bending tests were designed and carried out to experimentally characterize the deformed shapes and force-deflection responses of wires and TWBs (cf. Fig. 1c), which were then utilized to calibrate and validate reduced-order FE models (cf. Fig. 1d and f). As shown in Fig. 1e, we also developed and calibrated/validated high-fidelity FE models of TWBs as virtual surrogates for experimental testing. In these models, in addition to the non-linear geometrical and material behaviors, other sources of nonlinearity such as contact and friction along wire-wire and wire-tape interfaces are considered. More details regarding both reduced-order and high-fidelity

FE models, as well as their generalization to enable modeling CWBs and branching wire harnesses are presented in Sections 4 and 5, respectively.

The remainder of this manuscript is organized as follows: In Section 2, we describe the tensile tests conducted to experimentally characterize the mechanical behavior of various CWB components. We also utilize three-point bending tests to determine the force-deflection response of CWBs, as well as customized bending tests for branching wire harnesses to characterize the behavior of the branch break-out joint. In Section 3, we employ 3D FE modeling together with an optimization based algorithm to calibrate elastoplastic properties of CWB components based on experimental data. The high-fidelity and reduced-order models used for simulating the mechanical behavior of CWBs are described in Section 4. In that section, we also describe the calibration and validation of each model. A similar line of study is presented in Section 5 for characterizing the behavior of branch break-out joint in wire harnesses, where we show it is essential to implement a viscoelastic material model to accurately simulate its bending response. Final concluding remarks are presented in Section 6.

2. Experimental testing

Elastoplastic material properties of harness components such as protective conduits, and tapes are required for 3D FE modeling of wire

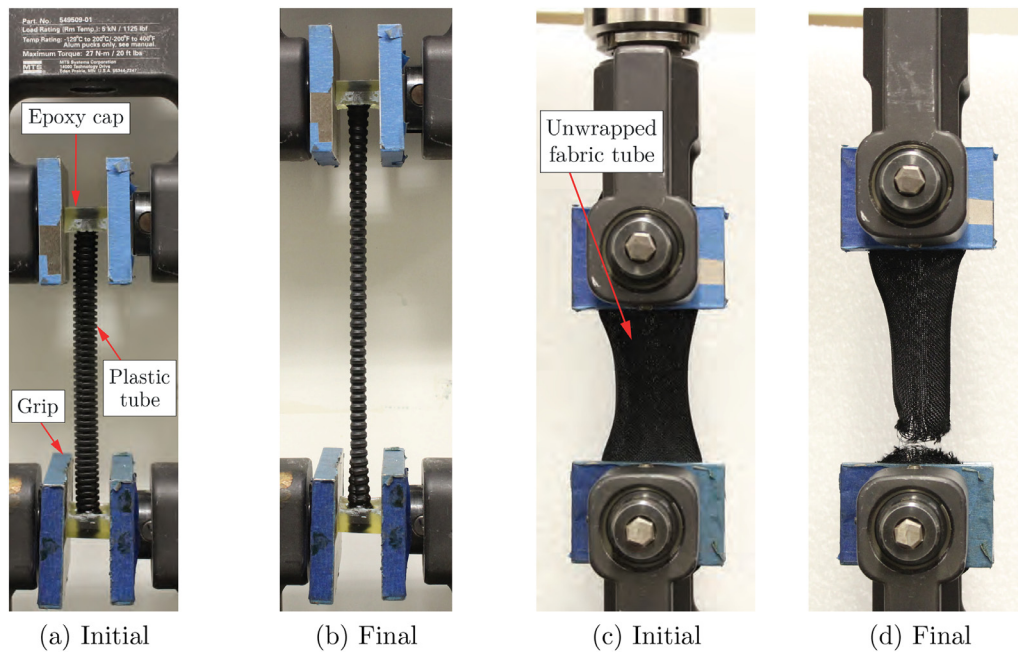


Fig. 2. Initial and final shapes of (a,b) plastic tube and (c,d) unwrapped fabric tube samples during tensile tests.

harnesses. The properties are determined by using an optimization algorithm on tensile test data of the harness components. Then, the effective elastoplastic properties of CWBs are determined by simulating the bending response of CWB samples and comparing the simulation result against the measured response of CWB samples from three-point bending experiments. Sample preparation, and a description of the experimental setup for all the tests conducted are presented in this section.

2.1. Protective tubes: tensile tests

Plastic tube samples are prepared for tensile testing by cutting pieces off the spool and casting the ends of the tubes in epoxy. Two types of plastic tubes are tested, which will be referred to as closed and open tubes, with the latter having a cut along the longitudinal axis to facilitate installing around wires. The diameter of each sample is 10 mm and the gauge length is 114.3 mm (4.5 in), which is extended by 50 mm at a rate of 0.423 mm s^{-1} (1 min^{-1}). A Test Resources load frame is used to conduct the tests and samples are mounted by clamping the epoxy casts with MTS Advantage screw action grips. The experimental setup is shown in Fig. 2a and b.

The fabric tube is a self-wrapping sleeve woven with polyethylene terephthalate (PET) yarn, which has an architecture similar to textile fabrics. Therefore, the sample dimensions and test parameters are chosen based on the ASTM D5034-09 standard for determining breaking strength and elongation of textile fabrics. The total sample length is 200 mm and the gauge length is 75 mm. An MTS C43.504 load frame is used to conduct the tests and samples are unwrapped before mounting with MTS screw action grips. The sample is extended at a rate of 5 mm s^{-1} until breakage. The experimental setup for this tensile test is shown in Fig. 2c and d.

2.2. CWBs: three-point bending test

The bending response of CWBs is characterized by conducting three-point bending tests on custom-made samples, which are prepared in a three-step process. First, pieces of electrical wire are cut off from a spool and straightened. A protective tube is then fitted around the wire bundle and finally the straightened wires and the tube are taped together at the ends. For CWB samples using the open plastic tube, an

additional layer of tape is applied along the length of the tube. It could be applied as either *coarse taping*, which refers to a helical-shaped taping with distance between each wrap, or *half-lap* taping, in which each helical wrap overlaps with half of the width of the previous wrap. All CWBs tested in this study have 19 electrical wires, which could be two distinct types (referred to as type 1 and type 2) or a mixture of them. The protective covering is either a closed/open plastic tube or a fabric tube and, for CWBs with open plastic tube covering, either the coarse or half-lap taping could be applied. For each case, three samples are fabricated and tested to characterize the variability in resulting force-deflection responses due to uncertainty effects such as residual stresses or variations in the geometry of the samples.

Fig. 3a illustrates the experimental setup used for conducting three-point bending tests on CWB samples. Note that there is no standard for characterizing the bending behavior of these flexible composite structures. Therefore, we adopt the ASTM D790-17 standard for determining flexural properties of electrical insulation materials as a reference for choosing the sample length and the deflection rate. For a sample with a diameter of 10 mm, a length of 200 mm is chosen with a support span of 127 mm and an overhang of 36.5 mm on either side. The tests are carried out on an MTS C43.5045 load frame and CWB samples are mounted using MTS three-point bend fixtures with 5mm diameter roller pins. The sample is deflected at the center by 30mm at 0.5 mm s^{-1} . A Transducer Techniques MLP series load cell with 222.4N(50 lb) load capacity is used to measure the bending force and a dSPACE 1103 DAQ is used to record the force data. Additionally, 3 mm diameter IR reflective markers are placed along the length of the sample and an Optitrack motion capture system is utilized to measure the sample deflection and capture its bent shape during the test. Reflective parts of the test setup are covered with masking tape to prevent measurement noise. Fig. 3b and c show a larger view of the initial and final bent shapes, respectively, of the CWB sample.

2.3. Branching wire harness: customized bending test

The stiffness of the branch-out joint in a Y-shaped CWB sample is characterized by conducting bending tests, as shown in Fig. 4. In this branching wire harness, the main segment S1 is made of 38 wires enclosed in a 15mm diameter open plastic tube with coarse taping.

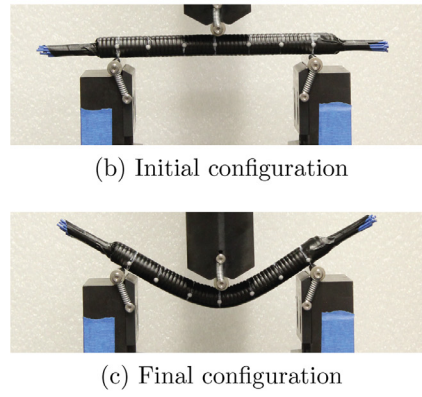
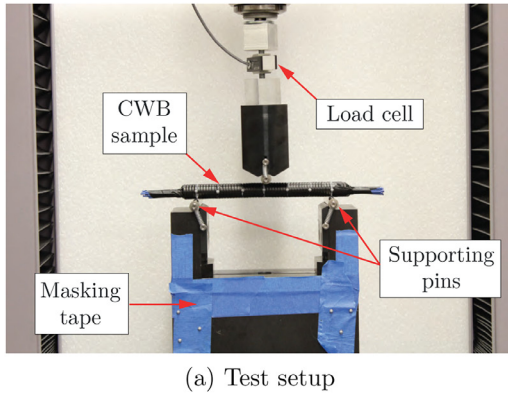


Fig. 3. (a) Three-point bending test setup for CWBs, showing the sample, load cell, and mounting fixtures; (b,c) Initial and bent shapes of the CWB sample.

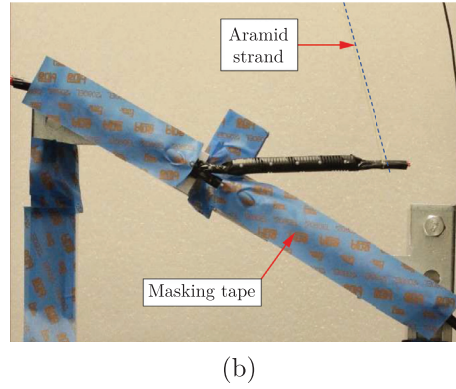
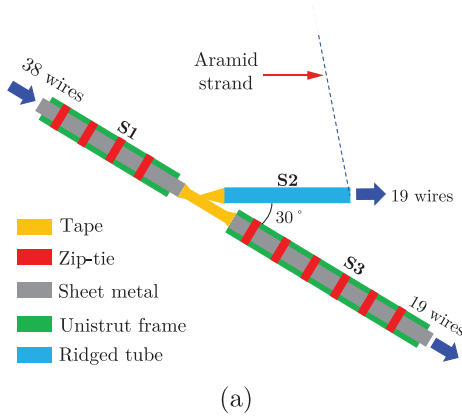


Fig. 4. (a) Schematic and (b) experimental setup for characterizing the bending response of branching CWB samples.

Segment S2 makes a 30° angle with segment S3 and both consist of 19 wires enclosed in 10mm diameter open plastic tubes. The ends of the harness and the exposed wires at the branch node are covered in half-lap tape. During the bending tests, segments S1 and S3 of the Y-shaped CWB are fastened to an aluminum unistrut frame using zip ties to create a fixed boundary condition. The frame is mounted on an MTS C43.504 load frame with clevis pin adapters. The end of segment S2 is connected to a Futek 8.9N(2 lb) load cell (mounted on the load frame cross-head) using an aramid strand. The cross-head is then displaced by 50 mm at 1 mm s⁻¹ and the tension measured in the aramid strand by the load cell is recorded using a dSPACE 1103 DAQ system. Motion capture markers are placed along segment S2 to measure vertical deflection of the free end and to capture the shape of this segment during the test.

3. CWB components: calibration of material properties

3.1. Constitutive model

The constitutive model characterizing the elastoplastic material behavior of CWB components is given by Simo and Hughes [34]

$$\sigma = \mathbb{C} : (\epsilon - \epsilon^p), \quad (1)$$

where σ is the Cauchy stress tensor, ϵ is the total strain tensor, ϵ^p is the plastic strain tensor, and \mathbb{C} is the fourth-order stiffness tensor. Given the assumption of isotropic properties for all CWB components, we can characterize arrays of \mathbb{C} using only two constants: the Young's modulus E and the Poisson's ratio ν . The yield stress σ_Y can then be evaluated using the von Mises yield criterion, i.e., when the second principal invariant of the deviatoric stress tensor s reaches a threshold value (J_2 flow theory) [35]. The stress tensor after the yield point is computed using a strain hardening law as Jirásek and Bazant [36]

$$\bar{\sigma} = \sigma_Y + K(\bar{\epsilon}^p)^n \quad \text{if } \bar{\sigma} \geq \sigma_Y, \quad (2)$$

where K and n are the strength coefficient and strain hardening exponent, respectively. Also, $\bar{\sigma} = (\frac{3}{2}s : s)^{\frac{1}{2}}$ and $\bar{\epsilon}^p = \int d\bar{\epsilon}^p$ are the effective stress and the effective plastic strain (cumulative measure of plastic strain increments $d\bar{\epsilon}^p$), respectively.

Before describing the calibration process, it is worth mentioning that material properties of two CWB components, namely the electrical wires and the PVC tape, have already been determined during our earlier study on TWBs [33]. Note that each single wire is in fact a flexible composite material composed of a helical stranded copper core and a polymeric insulation. Thus, its behavior subject to bending and tensile loads would be completely different due to the geometrical nonlinearity effects (e.g., friction between different components) and nonuniform plastic deformations under bending (see [33] for a detailed discussion). Since wires and wires harnesses are dominantly subject to bending loads during the assembly process, as shown in Fig. 1c, force-deflection curves obtained from cantilever bending tests (rather than tensile tests) are employed to calibrate their elastoplastic properties. Two types of wires are incorporated in CWBs studied in this work, which will be referred to as types 1 and 2. The outer diameter d_o of the polymer insulation and the diameter of the copper core d_c for each type of wire are given in Table 1. This table also shows the homogenized (effective) properties of these wires in bending, together with the elastoplastic tensile properties of the PVC

Table 1

Cross-section radii and homogenized elastoplastic material properties of two types of electrical wires in bending, as well as tensile properties of the PVC tape [33].

Component	d_c (mm)	d_o (mm)	E (MPa)	σ_Y (MPa)	K (MPa)	n
Type 1	0.85	1.25	5,641	4.95	850	0.78
Type 2	0.7	1.4	4,528	4.52	1,327	0.90
PVC tape	–	–	119	2.4	16.3	0.73

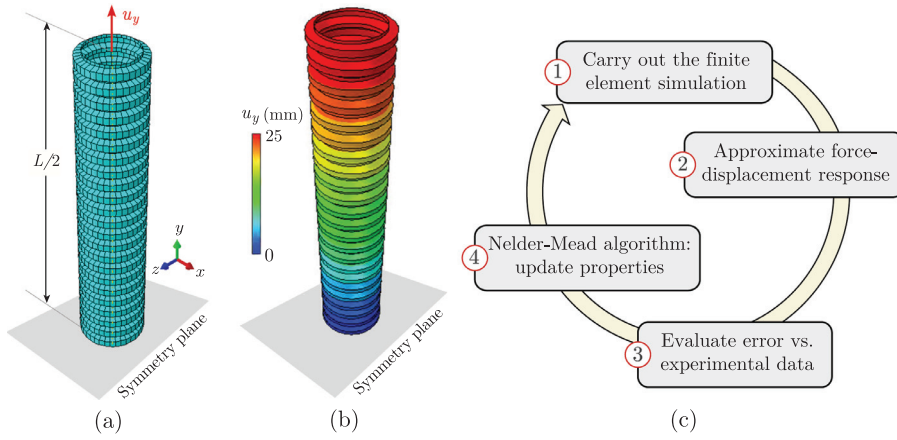


Fig. 5. (a) FE model of the closed plastic tube type with length $L = 12$ cm, inner diameter $d_i = 10.7$ mm, outer diameter $d_o = 14.1$ mm, and thickness $t = 0.27$ mm; (b) simulated displacement field subject to a tensile displacement in the y -direction; (c) schematic of the optimization-based approach for the calibration of material properties.

tape calibrated in [33]. Note that effective Poisson's ratio of wires are $\nu = 0.39$, and effective densities of wire types 2 and 3 are $\rho_2 = 4.34$ and $\rho_3 = 4.97$ g/cm³, respectively.

3.2. Calibration of material properties

In order to calibrate the elastoplastic properties (E , σ_Y , K , and n) of remaining CWB components, *i.e.*, closed/open plastic and fabric tubes, we use an optimization-based algorithm to minimize the error between their experimental and simulated tensile force-displacement responses. In this approach, high-fidelity FE models are created for each component and appropriate boundary conditions are applied to replicate tensile tests described in Section 2.1 (*cf.* Fig. 2). For example, Fig. 5a and b show the FE model and simulated axial displacement field in the closed plastic tube, where four-node finite strain shell elements are employed to discretize the domain. Note that only half of the tube is modeled due to the symmetry of the geometry and the tensile load during the physical test. Symmetric boundary conditions (BCs) are thus assigned to mesh nodes on the bottom face of the model, while the nodes on the upper face are constrained in the xz plane and subjected to displacement $u_y = 25$ mm. Note that a shell element has both translational and rotational degrees of freedom at each node and also takes into account the change of thickness due to in-plane deformations (membrane strain) [37,38]. Thus, to facilitate the numerical convergence, we apply in-plane displacement and rotational hourglass controls to these elements [39]. Also, five Gauss quadrature points are used in the through-the-thickness direction to accurately approximate the variation of thickness of shell elements during the simulation. It is noteworthy that all FE simulations presented in this work are carried out using the software package Abaqus [40].

The polypropylene ridged tube and polyester fabric tube have densities of 0.9 g/cm³ and 1 g/cm³, respectively. The optimization-based algorithm utilized for calibrating the elastoplastic properties of each component is schematically shown in Fig. 5c. The Nelder-Mead simplex optimization algorithm [41,42] is employed to calibrate E , σ_Y , K , and n for closed and open ridged tubes. The algorithm is integrated with the FE solver to automatically run tensile simulations and minimize the l_2 -norm of the error, $\|e\|_{l_2}$, between simulated and experimental force-displacement curves. The process begins with performing an FE simulation using initial estimates of material properties based on tensile stress-strain data reported in the literature for similar materials. For example, because the plastic tube is made of polypropylene, we have used the test data reported in [43] to obtain initial guesses for material properties. Note that for unwrapped fabric tubes, E and σ_Y values can easily be pre-determined based on the linear elastic regions of corresponding

experimentally measured tensile force-displacement curves as

$$E = \frac{FL}{u_y A}, \quad \sigma_Y = E \frac{u_y^{\text{dev}}}{L}, \quad (3)$$

where u_y is the displacement in the loading direction, F is the recorded applied force, L is the sample's length, and A is its cross sectional area. Also, u_y^{dev} is the displacement at which the force-displacement curve of the component deviates from a linear elastic response. Therefore, after performing the FE simulation using initial estimates of two parameters K and n , the force-displacement response is evaluated by summing approximated traction vectors at nodes where displacement BC is applied (*e.g.*, nodes on the upper face of the plastic tube model in Fig. 5a).

The Nelder-Mead simplex algorithm is a direct search method for solving unconstrained nonlinear multivariable optimization problems, meaning there is no need for the evaluation of gradients in this method. In the current study, we aim to minimize the objective function

$$\min \|e\|_{l_2}(\mathbf{v}_{\text{mat}}) = \min \|\mathbf{F}_{\text{exp}} - \mathbf{F}_{\text{FE}}(\mathbf{v}_{\text{mat}})\|, \quad (4)$$

where \mathbf{v}_{mat} is a vector holding material properties, while \mathbf{F}_{exp} and \mathbf{F}_{FE} are forces obtained from the experiment and the simulation, respectively. Assuming that the size of \mathbf{v}_{mat} is m (the number of material properties to be optimized), we first build a simplex in m -dimensional space based on initial estimates for each component. Note that an m -dimensional simplex is a geometric shape with $m + 1$ vertices, *e.g.*, a 3D simplex is a pyramid. The Nelder-Mead method uses an iterative approach to generate a sequence of simplices to search for an optimal solution for a given objective function (in this case, $\|e\|_{l_2}(\mathbf{v}_{\text{mat}})$). The algorithm builds the first simplex around the initial estimate for material properties $\mathbf{v}_{\text{mat},0}$ by adding 5% of each component $v_{\text{mat},0}(i)$ to $\mathbf{v}_{\text{mat},0}$. In each iteration, a new point in or near the current simplex is generated, and the worst vertex with the highest $\|e\|_{l_2}$ is replaced with a better estimate by applying reflection, expansion, contraction, and shrink transformation operations to the simplex. This iterative process stops when the size of the current simplex becomes excessively small or $\|e\|_{l_2}$ converges to the user-defined tolerance value.

As shown in Fig. 6a, there is a perfect agreement between these curves for the closed plastic tube after the completion of the calibration process, with the calibrated properties reported in Table 2. It is worth mentioning that because the Poisson's ratio of CWB components has a negligible impact on simulation results, we directly use the values reported in the literature for corresponding polymers (*e.g.*, $\nu = 0.42$ of polypropylene for the plastic tube).

Fig. 6a and Table 2 also show the force-displacement response of the open plastic tube and corresponding calibrated material properties evaluated using the optimization-based algorithm, respectively. The top view (xz -plane) of the FE simulation of the deformed shape of this tube subject to a tensile displacement of $u_y = 25$ mm is also illustrated in

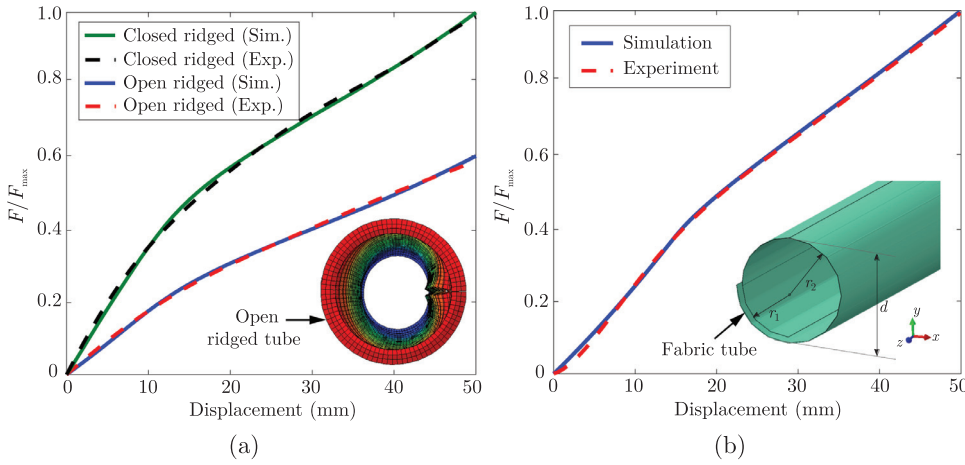


Fig. 6. Comparison of experimental versus simulated force-displacement responses subject to a tensile load in the axial direction after the calibration of material properties: (a) closed and open plastic tubes, also showing the top view of the FE simulation for the latter; (b) fabric tube, where $r_1 = 4.7$ mm, $r_2 = 5.3$ mm, $d = 10.6$ mm. Length, width, and thickness of unwrapped fabric tube samples are $L = 150$ mm, $w = 49$ mm, and $t = 0.6$ mm, respectively.

Table 2

Calibrated elastoplastic material properties of protective coverings of CWBs evaluated using the optimization-based algorithm.

Component	E (MPa)	σ_y (MPa)	K (MPa)	n
Closed plastic tube	1,559	8.6	25.6	0.12
Open plastic tube	698	8.8	23.1	0.83
Fabric tube	93.5	10.0	30.8	0.60

this Fig. 6a, where self-contact is considered between elements along the longitudinal cut. Although all geometrical features of the closed and open plastic tubes are identical, a significant difference is observed between their force-displacement curves in Fig. 6a. This behavior is not attributed the longitudinal cut in the open plastic tube, as numerical simulations show that the presence this cut does not have a notable impact on the force-displacement response under this type of loading. Instead, this difference emanates from different material properties of the closed and open tubes (cf. Table 2), which is confirmed experimentally by the higher density of the former.

Calibrated elastoplastic properties of the fabric tube (made of polyester, $\nu = 0.4$) are also given in Table 2. Fig. 6b shows that good agreement is achieved between simulated and experimental force-displacement responses of this component after calibrating its properties. This figure also illustrates the geometry of this tube, which includes 1.25 wraps of fabric. However, as noted in Section 2.1, the tensile test is conducted on a $150 \text{ mm} \times 49 \text{ mm}$ unwrapped rectangular sample. The corresponding FE model is discretized using shell elements (thickness: $t = 0.6$ mm). Note that during the calibration process, it is assumed that the fabric tube has isotropic material properties, although it is known that a fabric material can have different properties in the weft and warp directions. In Section 4.2, we show that using an orthotropic constitutive model is indeed essential for the accurate approximation of the deformation response of CWBs with a protective fabric tube. Therefore, the properties reported in Table 2 for this tube are only associated with the warp direction. However, given its small width and more importantly the pre-twist in the weft direction, it would not be feasible to perform a tensile test and calibrate corresponding properties due to stress concentrations near the grip and the effect of residual stresses. Thus, as will be discussed in Section 4.2, these properties are calibrated by matching simulated and experimental force-deflection responses obtained from a three-point bending test for the corresponding CWB.

4. Simulating the bending response of CWBs

In this section, we implement high-fidelity and reduced-order FE models to analyze the bending response of CWBs and calibrate/validate results with experimental data. Note that for applications such as digital

manufacturing and VR, only the reduced-order FE model would be of interest. This is due to the significantly lower computational cost of such analysis compared to a high-fidelity FE simulation without compromising the accuracy, which will be shown later in this section. However, given the exceedingly large number of design permutations for a CWB governed by various types/number of wires, type/pattern of taping, and type/size of protective tubes, it would not be feasible to perform the bending tests needed to calibrate a reduced-order model for all constructions. A high-fidelity FE model can thus serve as a surrogate for expensive and time-consuming experimental testing by virtually simulating the bending response of a CWB using already calibrated properties of each component and parameters governing their interaction. Therefore, we must also calibrate these parameters, including friction coefficients between different components and the cohesive strength along the tape-tube interface with force-deflection responses obtained from three-point bending tests. Next, we provide more details regarding FE models, the calibration process, and the validation of results with experimental data.

4.1. High-fidelity FE model of CWBs

Fig. 7 shows the high-fidelity FE model of a CWB composed of 19 wires of type 2 embedded in a coarsely-taped open plastic tube. The boundary conditions are designed to replicate a three-point bending test described in Section 2.2, where two steel rollers on the bottom and a feeder at the top are placed in contact with CWB. The feeder moves downward to apply the bending load. The inset of Fig. 7 shows a portion of the conforming mesh generated to build the FE model, which consists of 8-node hexahedral elements (for wires) and 4-node shell elements (for tube and tape). The tube length, support span, and length of taped wires at the end are $l = 152.4$ mm, $L = 127$ mm, and $a = 38.1$ mm, respectively. The coarse taping in this case has a helical shape consisting of only one layer of PVC tape with thickness $t = 0.1$ mm, radius $r = 7.1$ mm, width $w = 18.8$ mm, and helix pitch of $p = 2w$. The shape of this tape can analytically be characterized as

$$\begin{Bmatrix} x \\ y \\ z \end{Bmatrix} = \begin{Bmatrix} r \cos(\frac{2\pi}{p}u) \\ r \sin(\frac{2\pi}{p}u) \\ u \end{Bmatrix} = \begin{Bmatrix} r \cos(\frac{\pi}{w}u) \\ r \sin(\frac{\pi}{w}u) \\ u \end{Bmatrix}, \quad (5)$$

$u \in [0, L - w]$.

As noted previously, the high-fidelity simulation of the mechanical behavior of CWBs requires taking into account contact and friction between wire-wire and wire-tube. Further, this model must consider contact and friction between steel rollers and the coarsely-taped tube, which could either be the roller-tape or the roller-tube. To simulate these interactions, we employ an isotropic Coulomb frictional contact model between various components. The Coulomb friction model relates the

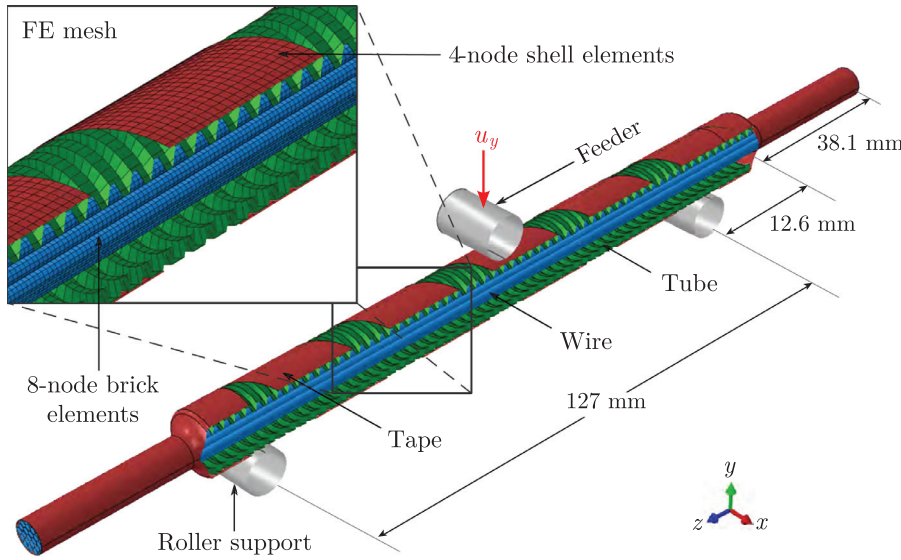


Fig. 7. 3D FE model of a composite wire bundle (CWB) composed of 19 wires of type 2 in a coarsely-taped open plastic tube. The inset shows 8-node hexahedral and 4-node shell elements used in the FE model for discretizing wires and tube/tape, respectively.

normal stress σ to the shear stress τ along a contact interface as $\tau = \mu\sigma$, where μ is the friction coefficient [44]. For friction between wires, we employ a dynamic friction model, in which the friction coefficient varies versus the slip rate from sticking (static, μ_s) to slipping (kinetic, μ_k) exponentially as [45]

$$\mu = \mu_k + (\mu_s - \mu_k)e^{-d_c \dot{\gamma}}, \quad (6)$$

where d_c is the decay coefficient and $\dot{\gamma} = \sqrt{\dot{\gamma}_1^2 + \dot{\gamma}_2^2}$ is the equivalent slip rate. In the latter, $\dot{\gamma}_1$ and $\dot{\gamma}_2$ are two slip velocities along local tangent directions of the contact surface between adjacent wires.

The adhesive bonding between tapes and either wires or tubes is modeled using a cohesive-contact model taking into account interfacial damage (debonding) at large deformations. In this surface-based cohesive model, a linear elastic traction-separation law describes the interfacial behavior before the initiation of damage. An interface stiffness tensor K_{ij} is employed to relate the element traction vector t_i to the relative separation of points located on opposing sides of the interface, $\delta_j = u_j^+ - u_j^-$, as [46,47],

$$t_i = K_{ij} \delta_j = K_{ij} (u_j^+ - u_j^-), \quad (7)$$

where $i/j = n, s, t$ correspond to displacements along normal (n) and shear (s, t) directions. Note that in this traction-separation law normal and tangential stiffness components are uncoupled, meaning all off-diagonal component of the stiffness matrix are zero ($K_{ns} = K_{nt} = K_{st} = 0$) and only diagonal components K_{nn} , K_{ss} , and K_{tt} need to be calibrated.

A damage model is also utilized to simulate the debonding occurring along tape and wire/tube interfaces at large deformations. A maximum separation criterion is used to determine the onset of the interfacial damage, which can be described as [48]

$$\max\{\delta_n, \delta_s, \delta_t\} = \{\delta_n^0, \delta_s^0, \delta_t^0\}. \quad (8)$$

The damage evolution (softening) is then simulated as

$$t_i = (1 - D)t_i^*, \quad (9)$$

where D is the damage parameter varying between 0 (undamaged) and 1 (fully damaged). Also, t_i^* are components of the contact traction vector evaluated based on the elastic traction-separation law. An exponential decay function is defined to characterize the evolution of D as [48]

$$D = 1 - \left(\frac{\delta_m^0}{\delta_m} \right)^{\alpha} \left[1 - \frac{1 - e^{-\alpha \left(\frac{\delta_m - \delta_m^0}{\delta_m^0 - \delta_m^0} \right)}}{1 - e^{-\alpha}} \right], \quad (10)$$

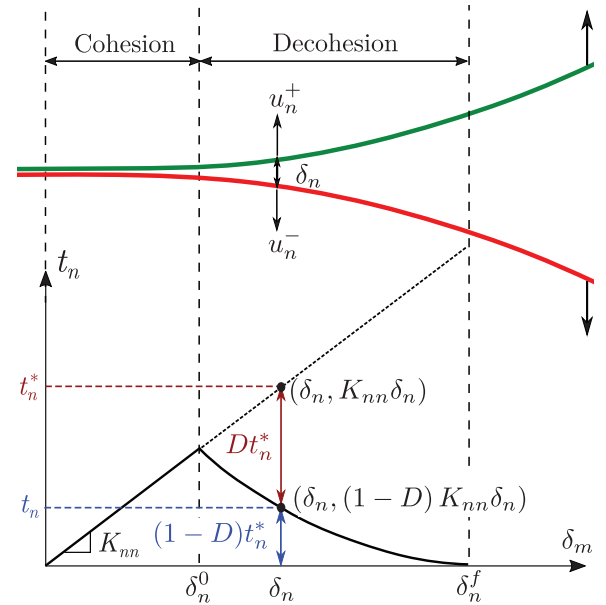


Fig. 8. Traction-separation cohesive response with exponential damage evolution in normal direction to contact surfaces at interface.

where α is the damage evolution rate, $\delta_m = \sqrt{\langle \delta_n \rangle^2 + \delta_s^2 + \delta_t^2}$ is the effective separation, and δ_m^0 and δ_m^f are initial (at the onset of damage) and final (at failure) effective separations, respectively. The cohesive response and damage evolution for the case of normal separation ($\delta_m = \delta_n$) across the interface is schematically shown in Fig. 8.

The severe nonlinearity imposed by contact-friction and cohesive damage in high-fidelity FE models of CWB, as well as the elastoplastic material behavior of its components, make it practically impossible to simulate the bending response using an implicit integration scheme. This is due to the exceedingly small (i.e., smaller than the machine precision) displacement increment needed to approximate the next converged solution at each step of the Newton-Raphson iteration, which prohibits convergence [49]. In order to resolve this issue, we implement an explicit dynamic integration scheme, which is a conditionally stable algorithm [50]. The stable time increment in this approach can be estimated by relating the elastic wave speed to the size and density

of elements as [51]

$$\Delta t_{\text{stable}} = \frac{\min(L_e)}{C_d} = \min(L_e) \frac{\sqrt{\rho(1+\nu)(1-2\nu)}}{\sqrt{E(1-\nu)}}, \quad (11)$$

where L_e is the characteristic length of each element, ρ is the density, and C_d is the dilatational wave speed. According to (11), we can increase Δt_{stable} (and thus reduce the computational cost) by artificially increasing the material density as $\rho' = f_m \rho$, where f_m is the mass scaling factor. Note that the increased weight associated with applying f_m leads to higher inertial forces during an explicit dynamic simulation. Therefore, given the quasi-static nature of three-point bending tests in the current study, an appropriate value of f_m must be determined such that the ratio of kinetic to internal energy during the simulation is negligible (in this work, <2%). Otherwise, the dynamic effects (waves propagation) in the system causes unphysical vibrations that leads to unrealistic bent shapes and force-deflection responses. After an extensive numerical study, the high-fidelity simulations presented hereafter are conducted over a time period of $t = 1$ s with $f_m = 25$ to ensure that the impact of kinetic energy on accuracy is negligible.

4.2. Calibration/validation of high-fidelity models

4.2.1. CWBs with plastic tube protection

In order to calibrate the contact-friction and cohesive damage parameters used in high-fidelity FE models of CWBs with plastic tube protection, we aim to minimize the error between experimental and simulated force-deflection responses obtained from three-point bending tests. These parameters include friction coefficients associated with wire-wire μ_{ww} , roller-tube μ_{rtb} , and roller-tape μ_{rtt} , as well as K_{ii} , δ_m^0 , δ_m^f , and α characterizing the cohesion between tape and tubes. Note that values of μ_{ww} and K_{ii} have already been calibrated in our previous study focused on TWBs [33]. For the former, we consider a dynamic friction with $\mu_{\text{ww},s} = 0.4$, $\mu_{\text{ww},f} = 0.1$, and an exponential decay factor of $d_c = 2$, while for the latter $K_{nn} = 30 \text{ Nmm}^{-3}$ and $K_{ss} = K_{tt} = 30 \text{ Nmm}^{-3}$. Also, elastoplastic material properties of each component of CWBs are either determined in [33] (wires and the PVC tape) or characterized in Section 3.2 (protective tubes).

In order to calibrate the remaining parameters, we compare experimental and computational force-deflection responses of three CWBs, all composed of 19 wires of type 2 but with different protections: closed plastic tube, open plastic tube with half-lap taping, and open plastic tube with coarse taping. The bent shape of the former CWB after the completion of the calibration process is illustrated in Fig. 9. To determine appropriate values of μ_{rtb} and μ_{rtt} , we use the steel-polymer friction coefficient given in [52] as the initial estimate. Since in CWB with the closed plastic tube the roller is only in contact with the tube (no taping along its length, see Fig. 9), we use this model to calibrate μ_{rtb} . The CWB model with the half-lap taping on the open plastic tube is then

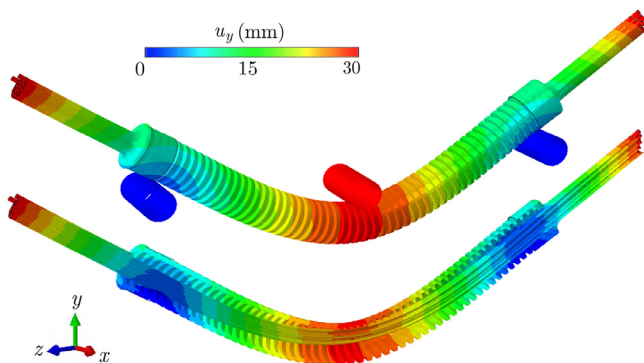


Fig. 9. High-fidelity FE simulation of the bent shape of a CWB composed of 19 wires of type 2 embedded in a closed plastic tube.

utilized to calibrate μ_{rtt} . The first two models are also used to calibrate cohesive damage parameters, noting that debonding along the tape and tube interface only occurs at large deformations. Thus, the initial portion of the force-deflection curve ($\delta_{\text{tip}} < 20$ mm) can be used to calibrate the friction coefficient and the remaining part of this curve will be used to calibrate cohesive damage parameters.

Fig. 10 provides a comparison between simulated and experimental force-deflection responses of CWB with a closed plastic tube protection, which is used for calibrating μ_{rtb} . As shown in the figure, $\mu_{\text{rtb}} = 0.3$ is a good estimate for this parameter. This plot also illustrates the effect of static and dynamic friction coefficients along wire-wire interfaces, indicating that the latter can better replicate experimental results. Further, using a dynamic friction model leads to wires sliding out of the hanging taped region at the two end of the sample (cf. Fig. 9), which is also observed in three-point bending tests. Note that the high-fidelity FE model considers the contact and friction between upper region of the tube and the embedded wire after bending as well. However, our numerical study shows that the friction coefficient associated with this interaction has a negligible impact on simulation results. The reason is that this contact-friction phenomenon only occurs at large deformations and only a small portion of the tube contacts the wires.

As depicted in Fig. 11a, a similar study is conducted on the CWB with half-lap taped open plastic tube protection to calibrate the friction coefficient between the roller and the PVC tape as $\mu_{\text{rtt}} = 0.1$. Several studies were also conducted on both CWBs to characterize the cohesive damage parameters that minimize the error between simulated and experimental force-deflection curves for $\delta_{\text{tip}} > 20$ mm, where debonding was observed between the tape and tube in three-point bending tests. According to this study, we will use $\delta_n^0 = \delta_s^0 = \delta_t^0 = \delta^0 = 0.03$ mm, $\delta_m^f = 0.08$ mm, and $\alpha = 2$ in the cohesive elements created along tape-tube interfaces.

The calibrated values of μ_{rtb} and μ_{rtt} , as well as the cohesive damage parameters are then used to validate the high-fidelity FE model by simulating the three-point bending response of a CWB composed of 19 wires of type 1 embedded in a coarsely-taped open plastic tube. The simulated bent shape of this CWB is illustrated in Fig. 12, in which some of the wires slide out of the taped regions at the two hanging ends (also observed experimentally). As shown in Fig. 11b, a good agreement is achieved between simulated and experimentally measured force-deflection responses of this CWB. Note that there is a notable variability between three experimental test results in this figures (and previous two curved used for the calibration of model), which is attributed to uncertainty factors such as residual stresses and variation in taping. Therefore, the small difference between the simulated force-deflection curve and the average of its experimental counterparts indicates that the high-fidelity FE model can serve as a reliable surrogate for laborious experimental testing for characterizing the bending response of CWBs.

4.2.2. CWBs with fabric tube protection

We have also simulated the bending response of a CWB composed of 19 wires of type 2 wrapped in a fabric tube to calibrate its non-isotropic material properties. In the corresponding high-fidelity FE model, we must consider self-contact for the fabric tube, which has 1.25 wraps around wires. The simulated deformed shape of this CWB is illustrated in Fig. 13, showing that the PVC tape is only applied at the two hanging ends. As shown in this figure, the wires again slide out of this taped region due to debonding of the adhesive tape, which is simulated using the cohesive damage parameters calibrated in Section 4.2.1. However, as shown in Fig. 14a, there is a significant discrepancy between the simulated and experimental force-deflection responses of this CWB when an isotropic material model is used for the fabric tube. This assumption is indeed unrealistic due to different elastic moduli of fabric in the warp and weft directions (E_1 and E_2), while only the former was calibrated in Section 3.2 ($E_1 = 93.5$ MPa). In the FE model, we can incorporate this behavior using plane stress shell elements with an orthotropic elastic material behavior for discretizing the fabric, which also requires calibrating its elastic modulus in the weft direction (E_2). The strain-stress

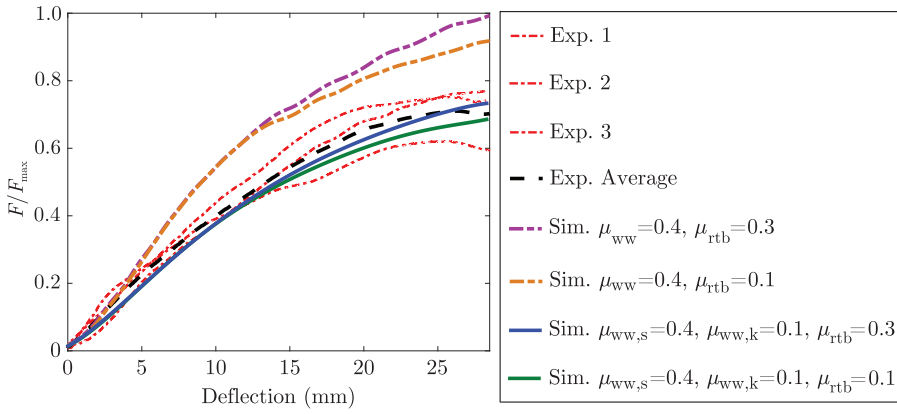


Fig. 10. Comparison of experimental and simulated force-deflection responses of a CWB composed of 19 wires of type 2 with a closed plastic tube protection for calibrating friction coefficients between wire-wire and roller-tube.

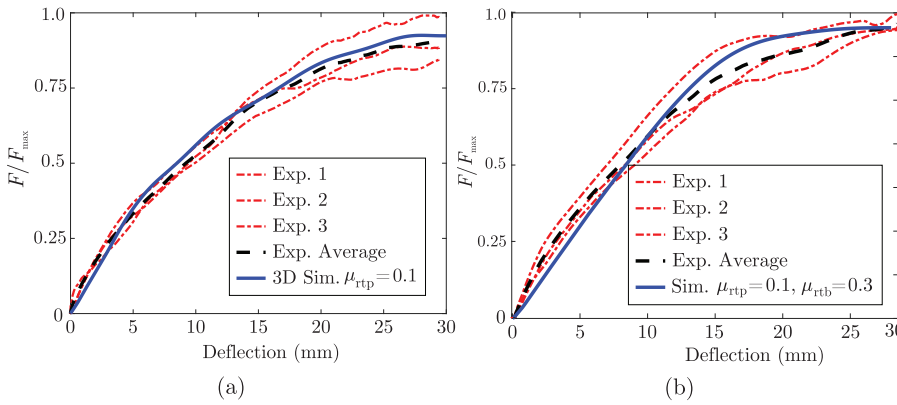


Fig. 11. Comparison between experimental and simulated force-deflection responses from three-point bending tests for (a) calibration of μ_{rtp} in a CWB composed of 19 type 2 wires within a half-lap taped tube; (b) validation of all calibrated parameters in the same CWB but with a coarsely-taped open plastic tube protection.

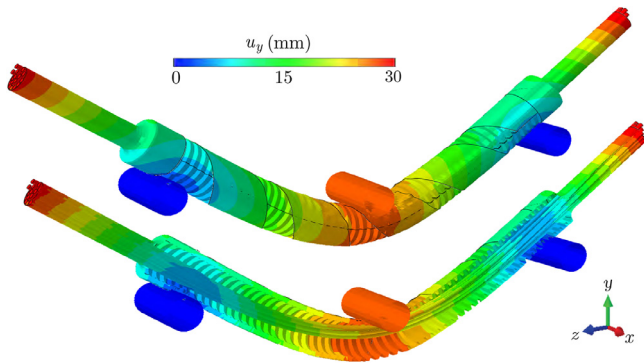


Fig. 12. 3D FE approximation of the bent shape of a CWB composed of 19 type 3 wires within a coarsely-taped open plastic tube type.

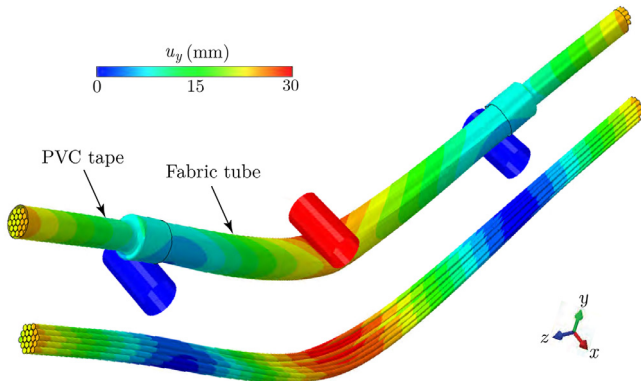


Fig. 13. High-fidelity FE simulation of the bent shape of a CWB composed of 19 type's wires wrapped in the fabric tube.

relation of a shell with orthotropic elastic properties under the plane stress assumption can be written as [53]

$$\boldsymbol{\varepsilon} = \begin{Bmatrix} \varepsilon_{11} \\ \varepsilon_{22} \\ \gamma_{12} \end{Bmatrix} = \begin{bmatrix} 1/E_1 & -\nu_{12}/E_1 & 0 \\ -\nu_{12}/E_1 & 1/E_2 & 0 \\ 0 & 0 & 1/G_{12} \end{bmatrix} \begin{Bmatrix} \sigma_{11} \\ \sigma_{22} \\ \sigma_{12} \end{Bmatrix}. \quad (12)$$

As shown in Fig. 14a, a parametric study indicated that using $E_2 = 0.6E_1$, together with $\nu_{12} = \nu = 0.4$ and $G_{12} = \frac{0.5(E_1+E_2)}{2(1+\nu_{12})}$, yields an excellent agreement between simulated and experimental force-deflection curves.

The calibrated elastic moduli of the fabric, together with other parameters calibrated in Section 4.2.1 are further validated by simulating the three-point bending response of a CWB composed of a mixture of 10 wires of type 1 and 9 wires of type 2 wrapped in a fabric tube. As depicted in Fig. 14b, an acceptable agreement is achieved between simulated and experimental force-deflection responses for this CWB. This observation once again shows the applicability of the high-fidelity FE model as a reliable surrogate to costly experimental testing for characterizing the bending response of CWBs.

4.3. Reduced-order FE model of CWBs

As shown in Section 4.2, the high-fidelity FE model can accurately predict the mechanical behavior of CWBs subject to a bending load, which is the dominant loading during the harness installation. However, despite using an explicit dynamic approach, such nonlinear 3D FE simulations are still highly computational demanding and must be carried out on massively parallel computing platforms. For example, the simulation shown in Fig. 13 (19 wires, fabric tube) is performed in 281 min (wall time) on 192 Intel Xeon x5650 processors at the Ohio Supercomputer Center (OSC). Clearly, such a huge computational burden prohibits the use of this model for applications such as digital manufacturing

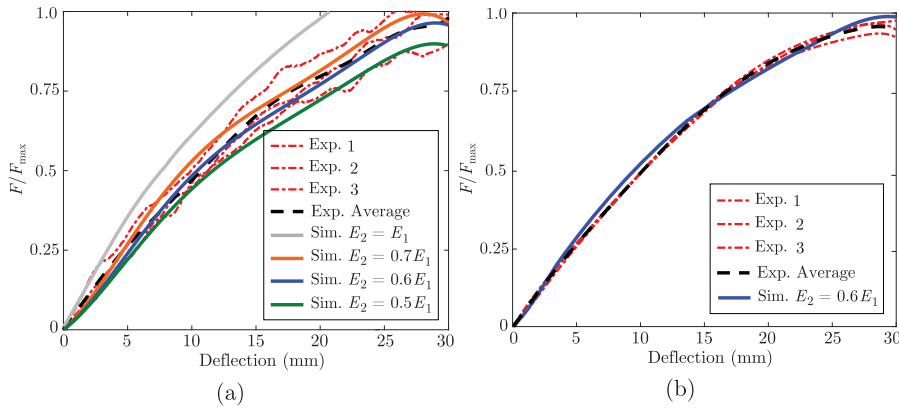


Fig. 14. Comparison between experimental and simulated force-deflection responses from three-point bending tests for (a) calibration of the transverse elastic modulus of the fabric tube used as protection material for a CWB composed of 19 wires of type 2; (b) validation of this parameter for a CWB composed of 10 wires of type 1 and 9 wires of type 2 with a fabric tube protection.

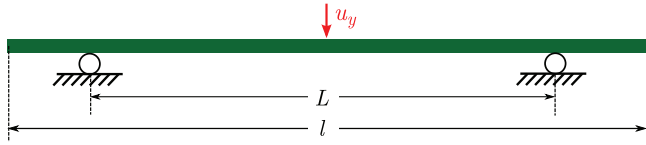


Fig. 15. Schematic of the reduced order FE model of the three-point bending test, where 1D beam elements are used for discretizing CWB.

and VR, which demand near real-time simulations. Instead, the main purpose of developing a high-fidelity model is to determine the force-deflection response of CWBs with various size/types of wires, protective tubes, and taping. This could lead to thousands of design permutations, which would clearly be impossible to characterize purely via experimental testing.

To address the challenges associated with the high computational cost of high-fidelity models for real-world applications, we use the force-deflection curve predicted by this model to calibrate a reduced-order FE model of CWBs relying on beam elements. We assign effective elastoplastic bending properties of CWB to each 1D beam element; thus by homogenizing its internal architecture we can avoid the costly modeling of contact-friction and cohesive damage. This in turn resolves the convergence difficulties arising in high-fidelity simulations, allowing the use of an implicit integration scheme in the reduced-order model. Similar to the material model used for each component of CWB, we implement a J_2 plasticity model (von Mises yield criterion) for each effective beam element. The calibration process is similar to that used for TWBs in [33], in which the elastic beam theory is used to first calibrate homogenized E_{eff} and σ_Y for a 1D model of the three-point bending test (cf. Fig. 15). In this approach, the linear elastic region of the force-deflection curve obtained from a high-fidelity simulation is employed to evaluate E_{eff} and σ_Y as

$$E_{\text{eff}} = \frac{FL^3}{48u_y I}, \quad \sigma_Y = \frac{F_{2\%} L}{\pi r_o^3}, \quad (13)$$

where L is the support span, F is the applied force at mid-span, r_o is the outer radius of CWB, $I = \frac{\pi r_o^4}{4}$ is its second moment of inertia, and $F_{2\%}$ is the applied force corresponding to $u_y = 0.02L$. Note that selecting $F_{2\%}$ for defining the yield point is conducted based on a parametric study, after which a notable deviation from the elastic material response was observed considering the geometrical nonlinearity.

The remainder of the calibration process is similar to that described in Section 3.2 (cf. Fig. 5c), where the Simplex optimization algorithm is utilized to determine K and n by minimizing the L_2 -norm of the error between reduced-order and high-fidelity simulated force-deflection curves. The resulting calibrated effective elastoplastic properties of CWBs studied in Section 4.2 are presented in Table 3, for which corresponding force-deflection curves perfectly match those obtained from

3D simulations. Note that each reduced order simulation can be carried out using an implicit integration scheme on a single processor in less than 22 seconds, which is a huge reduction in the computational cost compared to high-fidelity simulations without compromising the accuracy.

5. Simulating wire harness branching

While it is necessary to characterize the bending response of CWBs via high-fidelity FE simulations and subsequently determine their effective elastoplastic bending properties for reduced-order modeling, it is equally important to characterize the behavior of break-out joints in wire harnesses. As noted previously (cf. Fig. 4a), the protective tube is discontinued near the break-out joint and multiple layers of half-lap taping is used to stabilize the wires in this region. Characterizing the bending and torsional stiffnesses of this node, which is provided by both wires and the tape, is of particular importance for establishing a reliable reduced-order FE model.

In this section, we use both high-fidelity and reduced-order models to study the behavior of branching wire harnesses and calibrate/validate them with experimental data obtained from bending tests. The models created for each case are illustrated in Fig. 16, which correspond to the Y-shaped harness experimentally characterized in Section 2.3 and schematically shown in Fig. 4. In this branching harness, the main CWB segment is composed of 38 wires of type 2 embedded in a coarsely-taped open plastic tube, which is subdivided into two branches each consisting of 19 wires and forming a 30° angle with one another. Fig. 16a shows the locations at which the harness is fixed using zip-ties. To simulate the bending test, a tensile displacement is applied at the tip of the horizontal branch using a rigid link representing the aramid strand, which has a significantly higher stiffness than CWBs. Note that at the end of each branch, each CWB transitions into a half-lap taped TWB. We will use this test setup to calibrate FE models by matching simulated and experimental force-displacement responses measured at the end of the aramid strand (rigid link in the FE models).

A larger view of the high-fidelity FE model of the branching harness is illustrated in Fig. 17, which shows the hexagonal and shell elements used for discretizing the wires and tubes/tape, respectively. Note that material properties of all components, as well as contact-friction and cohesive damage parameters needed to simulate the mechanical behavior of this model are previously characterized. In the corresponding reduced-order model (cf. Fig. 16b), CWB and TWB portions of the branching harness are replaced with beam elements with pre-evaluated effective properties. A similar optimization-based approach as that described in Section 4.3 is employed to calibrate effective properties of the main CWB with 38 wires and TWBs. The branching point in the reduced-order analysis is modeled using elastic bushing-like connector elements, which can take into account three translational and three rotational stiffness values in a 3D space. Because connector elements at the

Table 3

Calibrated effective elastoplastic properties of CWBs in bending evaluated using the optimization-based algorithm. Values of E , σ_Y , and K are given in MPa.

CWB			E	σ_Y	K	n
#/type of wires	Tube	Taping				
19, type 2	closed plastic	–	15.7	0.6	1.59	0.3
19, type 2	open plastic	half-lap	20.6	0.35	4.3	0.24
19, type 2	open plastic	coarse	18.7	0.46	3.21	0.43
19, type 2	fabric	–	30.6	0.25	5.65	0.24
10 & 9, types 1 & 2	fabric	–	24.8	0.20	0.97	0.13

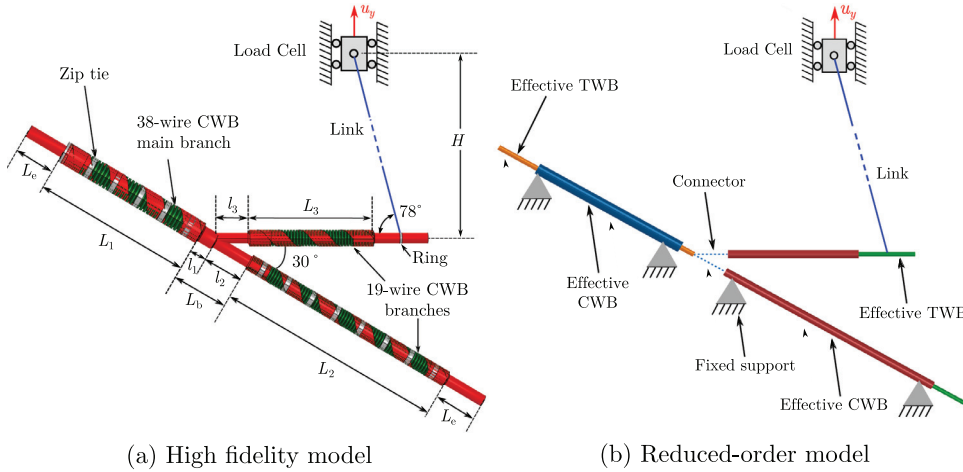


Fig. 16. FE models of the Y-shaped branching wire harness corresponding to experimental testing shown in Fig. 16 used the calibration of the branch break-out joint properties: $L_1 = 140$ mm, $L_2 = 203$ mm, $L_3 = 111$ mm, $L_e = 38$ mm, $l_1 = 13$ mm, $l_2 = l_3 = 30$ mm, and $H = 625$ mm.

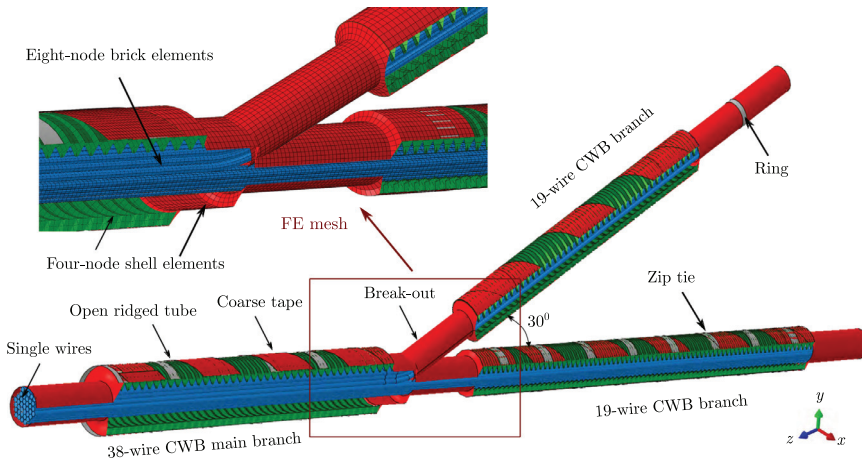


Fig. 17. 3D FE model of the branching wire harness, where the longitudinal cut shows the wires inside the protective plastic tube. Also, the inset shows 8-node hexahedral and 4-node shell elements used for discretizing wires and tape/tube, respectively.

branch break-out joint represent TWBs, we use effective elastic properties of each TWB (composed of either 38 or 19 wires) as stiffness values of bushing-like elements. The homogenized axial stiffness k , bending stiffness k_β , and torsional stiffness k_θ of TWBs can thus be evaluated using beam theory as

$$k = \frac{EA}{\lambda l}; \quad k_\beta = \frac{EI}{\lambda l}; \quad k_\theta = \frac{GJ}{\lambda l}, \quad (14)$$

where E is the elastic modulus, G is the shear modulus, A is the cross sectional area, I is the second moment of inertia, J is the polar moment of inertia, and $\lambda = \frac{l}{r}$ is the aspect ratio of TWB (l : length, r : radius of the circle circumscribing the cross section).

A comparison between high-fidelity and reduced-order simulated force-displacement responses of the branching wire harness is presented in Fig. 18a. The similarity of these curves once again shows the ability of the reduced order model to replicate the result obtained from a 3D FE analysis at a significantly lower computational cost. This similarity also verifies the use of an elastic bushing-like elements in the reduced-

order model despite using an elastoplastic model for wires and the tape in the high-fidelity model, meaning plastic deformations are negligible (corroborated by stresses developed in wires/tape). However, as shown in Fig. 18a, both simulated curves have a considerable discrepancy with the experimentally measured force-displacement response, especially in initial stages of the deformation ($u_y < 10$ mm). In other words, FE simulations cannot accurately predict the actual behavior of the branching harness in bending, although after the initial mismatch both experimental and numerical force-displacement curves follow the same trend.

The discrepancy between experimental and numerical force-displacement responses in Fig. 18a for $u_y < 10$ mm is attributed to the viscoelastic behavior of PVC tape layers at the branch break-out joint. Note that this elastomeric behavior was overlooked in characterizing the bending stiffness of CWBs and TWBs due to its negligible impact on the accuracy of simulations. This is because the main role of tape is to keep wires together and/or stabilize them within the protective tube; thus it does not have a notable contribution to the overall stiffness

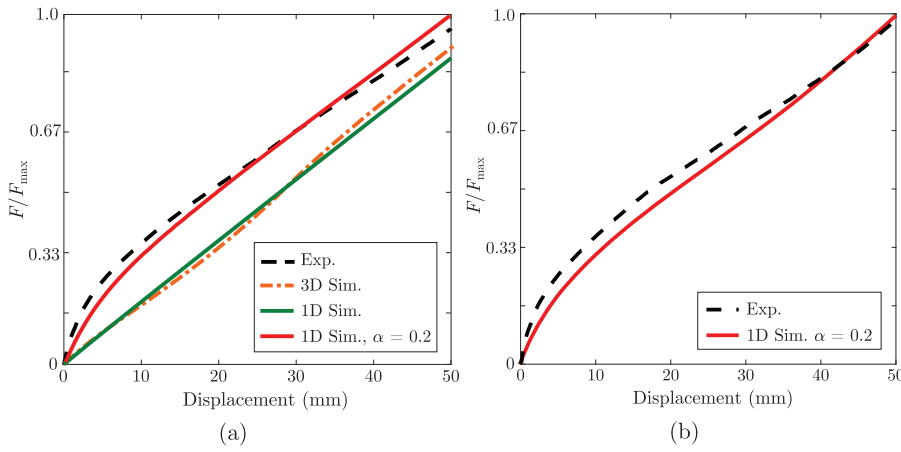


Fig. 18. Experimental and 3D/1D simulated force-displacement responses of branching wire harness bending tests for setups shown in (a) Fig. 16 and (b) Fig. 20.

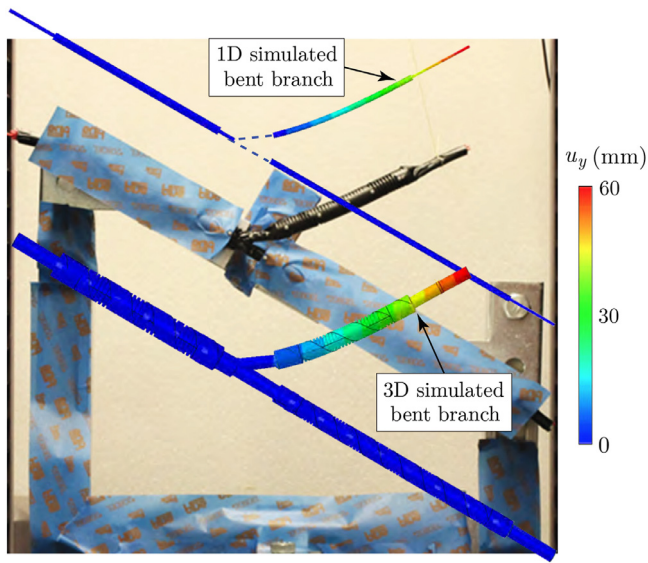


Fig. 19. Comparison between experimental, high-fidelity FE simulation, and reduced-order FE simulation of the bent shape of branching wire harness.

of CWBs/TWBs alone. However, in a branching wire harness, the tape layers wrapped around the break-out joint directly affect its torsional and bending stiffnesses. In order to simulate this viscoelastic behavior, we use the damping coefficient α to add the damping matrix \mathbf{C} to the dynamics governing equations as [49]

$$\mathbf{C} = \alpha \mathbf{K}, \quad (15)$$

where \mathbf{K} is the stiffness matrix. As shown in Fig. 18a, using this model with $\alpha = 0.2$ (calibrated via a parametric study) leads to an excellent agreement between simulated and experimentally measured force-displacement responses of the branching wire harness. A comparison between 1D/3D simulated bent shapes of the harness and the deformed shape observed in the cantilever bending test is provided in Fig. 19, which also shows a significant similarity.

In order to validate the viscoelastic model adopted for the break-out joint, we have tested/analyzed the bending response of the Y-shaped branching harness subject to a different loading condition. The reduced-order FE model of this bending test is illustrated in Fig. 20, where a vertical displacement is applied to the branch perpendicular to the plane of the wire harness. A comparison between simulated and experimental force-displacement responses of this test is depicted in Fig. 18b, showing a good agreement between both results using the calibrated damping coefficient $\alpha = 0.2$. This study not only validates the use of bushing-like

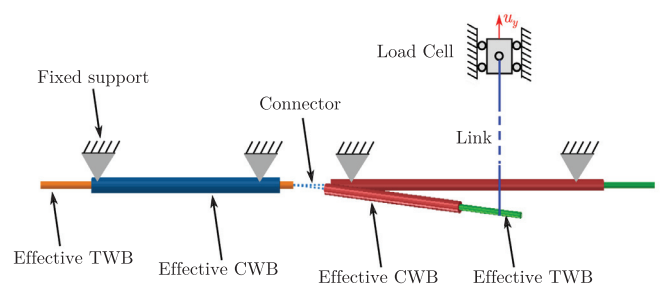


Fig. 20. Reduced-order FE model of the branching wire harness for the second loading condition, where the vertical displacement is applied through a rigid link (corresponding to the aramid wire) perpendicular to plane of the harness.

elements with viscoelastic properties for the branch break-out joint but also once again validates the use of beam elements with effective elastoplastic bending properties for modeling TWBs and CWBs in a complex branching wire harness.

6. Conclusion

High-fidelity and reduced-order FE models were presented to simulate the bending response of composite wire bundles (CWBs) and branching wire harnesses used for automotive applications. The high-fidelity model considers the elastoplastic material behavior of CWB components (wires, tape, protective tubes), together with wire-wire/tube contact-friction and tape-tube/wire cohesive damage. It was shown that after calibration with the experimental data obtained from tensile tests on each component and customized three-point bending tests on the whole CWB, this model can accurately predict the bending response of CWBs. High-fidelity FE analysis can thus serve as a reliable surrogate to laborious and costly experimental testing to characterize the force-deflection and deformed shape of CWBs in bending with large deformation. However, the high computational cost of such excessively nonlinear analyses is unacceptable for applications such as digital manufacturing and virtual reality, which aim to simulate the assembly of wire harnesses in real-time. We employed a reduced-order FE model relying on beam elements with homogenized elastoplastic bending properties (obtained using an optimization-based algorithm) to address this issue by significantly reducing the computational cost without undermining the accuracy. A similar line of study was then conducted to characterize the behavior of the break-out joint in branching wire harnesses, where we showed that a viscoelastic material model must be implemented to characterize its stiffness. In the reduced-order model, we simulated this behavior using bushing-like elements with damping, which also resulted

in a good agreement with experimentally measured force-displacement responses obtained from bending tests.

Acknowledgment

This work was funded by Honda R&D Americas, Inc. and also in part by an allocation of computing time from the Ohio Supercomputer Center (OSC) and the Ohio State University Simulation Innovation and Modeling Center (SIMCenter).

References

- Grégoire M, Schömer E. Interactive simulation of one-dimensional flexible parts. *Comput-Aided Des* 2007;39(8):694–707.
- Wakamatsu H, Hirai S. Static modeling of linear object deformation based on differential geometry. *Int J Robot Res* 2004;23(3):293–311.
- Hong K, Kiureghian AD, Sackman J. Bending behavior of helically wrapped cables. *J Eng Mech* 2005;131(5):500–11.
- Ghoreishi S, Cartraud P, Davies P, Messenger T. Analytical modeling of synthetic fiber ropes subjected to axial loads. Part I: a new continuum model for multilayered fibrous structures. *Int J Solids Struct* 2007;44(9):2924–42.
- Karathanasopoulos N, Ganghoffer J, Papailiou K. Analytical closed-form expressions for the structural response of helical constructions to thermal loads. *Int J Mech Sci* 2016;117:258–64.
- Cao X, Wu W. The establishment of a mechanics model of multi-strand wire rope subjected to bending load with finite element simulation and experimental verification. *Int J Mech Sci* 2018;142:289–303.
- Picinbono G, Delingette H, Ayache N. Real-time large displacement elasticity for surgery simulation: non-linear tensor-mass model. In: *Medical image computing and computer-assisted intervention—MICCAI 2000*. Springer; 2000. p. 643–52.
- Nikitin I, Nikitina L, Frolov P, Goebbels G, Göbel M, Klimenko S, et al. Real-time simulation of elastic objects in virtual environments using finite element method and precomputed Green's functions. In: *Eighth eurographics workshop on virtual environments*; 2002. p. 47–52.
- Ghoreishi S, Messenger T, Cartraud P, Davies P. Validity and limitations of linear analytical models for steel wire strands under axial loading, using a 3D fe model. *Int J Mech Sci* 2007;49(11):1251–61.
- Stanova E, Fedorko G, Fabian M, Kmet S. Computer modelling of wire strands and ropes part II: finite element-based applications. *Adv Eng Softw* 2011;42(6):322–31.
- Yu Y, Wang X, Chen Z. A simplified finite element model for structural cable bending mechanism. *Int J Mech Sci* 2016;113:196–210.
- Abdullah A, Rice J, Hamilton H, Consolazio G. An investigation on stressing and breakage response of a prestressing strand using an efficient finite element model. *Eng Struct* 2016;123:213–24.
- Wang X, Chen Z, Yu Y, Liu H. An innovative approach for numerical simulation of stress relaxation of structural cables. *Int J Mech Sci* 2017;131:971–81.
- Papailiou K. On the bending stiffness of transmission line conductors. *IEEE Trans Power Deliv* 1997;12(4):1576–88.
- Goss V, der Heijden GV, Thompson J, Neukirch S. Experiments on snap buckling, hysteresis and loop formation in twisted rods. *Exp Mech* 2005;45(2):101–11.
- Dörlich V, Hoffmann R, Linn J, Scheffer T, Diebels S. Towards viscoplastic constitutive models for Cosserat rods. *Arch Mech Eng* 2016;63(2):215–30.
- der Heijden GV, Neukirch S, Goss V, Thompson J. Instability and self-contact phenomena in the writhing of clamped rods. *Int J Mech Sci* 2003;45(1):161–96.
- Filiatrault A, Stearns C. Flexural properties of flexible conductors interconnecting electrical substation equipment. *J Struct Eng* 2005;131(1):151–9.
- Onur Y. Experimental and theoretical investigation of prestressing steel strand subjected to tensile load. *Int J Mech Sci* 2016;118:91–100.
- Nemov A, Boso D, Voynov I, Borovkov A, Schrefler B. Generalized stiffness coefficients for ITER superconducting cables, direct FE modeling and initial configuration. *Cryogenics* 2010;50(5):304–13.
- Foti F, di Roseto A. Analytical and finite element modelling of the elastic–plastic behaviour of metallic strands under axial–torsional loads. *Int J Mech Sci* 2016;115:202–14.
- Gautam M, Katnam K, Potluri P, Jha V, Latto J, Dodds N. Hybrid composite tensile armour wires in flexible risers: a multi-scale model. *Compos Struct* 2017;162:13–27.
- Vié M, Zufferey N, Cordeau J. Solving the wire-harness design problem at a european car manufacturer. *Eur J Oper Res* 2018.
- Park H, Lee S, Cuthosky M, et al. Computational support for concurrent engineering of cable harnesses. *Comput Eng* 1992;1. 261–261.
- Agard B, Tollenaere M. Design of wire harnesses for mass customization. In: *Recent advances in integrated design and manufacturing in mechanical engineering*. Springer; 2003. p. 53–62.
- Thonemann U, Brandeau M. Optimal commonality in component design. *Oper Res* 2000;48(1):1–19.
- Ng F, Ritchie J, Simmons J. The design and planning of cable harness assemblies. *Proc Inst Mech Eng Part B* 2000;214(10):881–90.
- Kikuchi M. Branch line apparatus for a wire harness and a method thereof. November 22 1994. US Patent 5,367,126.
- Toba K, Noro Y. Arranging method of a wire harness for a door. October 24 1995. US Patent 5,460,530.
- Saka K, Hashimoto M, Furuta K, Okamura T. Method of making a wire harness. February 4 1997. US Patent 5,598,627.
- Miyazaki T, Maeda Y, Hibasami A, Uchida M, Yamauchi M, Ito T, et al. Branch wire tie band, binding structure, and method of binding a wiring harness. April 14 2005. US Patent App. 10/882,182.
- Fukuda D. Method for manufacturing wire harness branching portion. December 1 2009. US Patent 7,624,503.
- Taghipour E, Vemula S, Wang Z, Zhou Y, Qarib H, Gargesh K, et al. Characterization and computational modeling of electrical wires and wire bundles subject to bending loads. *Int J Mech Sci* 2018;140:211–27.
- Simo J, Hughes T. *Computational inelasticity*, Vol. 7. Springer Science & Business Media; 2006.
- de Souza Neto E, Peric D, Owen D. *Computational methods for plasticity: theory and applications*. John Wiley & Sons; 2011.
- Jirásek M, Bazant Z. *Inelastic analysis of structures*. John Wiley & Sons; 2002.
- Hughes T, Liu W. Nonlinear finite element analysis of shells: part I. Three-dimensional shells. *Comput Methods Appl Mech Eng* 1981;26(3):331–62.
- Dvorkin E, Bathe K. A continuum mechanics based four-node shell element for general non-linear analysis. *Eng Comput* 1984;1(1):77–88.
- Zienkiewicz O, Taylor R, Too J. Reduced integration technique in general analysis of plates and shells. *Int J Numer Methods Eng* 1971;3(2):275–90.
- Systemès D. Abaqus version 2016, user documentation. Providence, RI: Dassault Systemes; 2016.
- Nelder J, Mead R. A simplex method for function minimization. *Comput J* 1965;7(4):308–13.
- Taghian J, Reeds J, Wright M, Wright P. Convergence properties of the nelder–mead simplex method in low dimensions. *SIAM J Optim* 1998;9(1):112–47.
- Zhao Z, Dong L, Chen L, Wang Y. Morphology development of pp/poe blends with high loading of magnesium hydroxide. *RSC Adv* 2015;5(23):17967–75.
- Zienkiewicz O, Taylor R. *The finite element method for solid and structural mechanics*. Butterworth-Heinemann; 2005.
- Oden J, Martins J. Models and computational methods for dynamic friction phenomena. *Comput Methods Appl Mech Eng* 1985;52(1-3):527–634.
- Borst RD, Pandolfi A. Finite-deformation irreversible cohesive elements for three-dimensional crack-propagation analysis. *Int J Numer Methods Eng* 1999;44(9):1267–82.
- Turon A, Davila C, Camanho P, Costa J. An engineering solution for mesh size effects in the simulation of delamination using cohesive zone models. *Eng Fract Mech* 2007;74(10):1665–82.
- Turon A, Camanho P, Costa J, Dávila C. A damage model for the simulation of delamination in advanced composites under variable-mode loading. *Mech Mater* 2006;38(11):1072–89.
- Bathe K. *Finite element procedures*. Klaus-Jurgen Bathe; 2006.
- Reddy J. *An introduction to nonlinear finite element analysis: with applications to heat transfer, fluid mechanics, and solid mechanics*. OUP Oxford; 2014.
- Borst RD, Crisfield M, Remmers J, Verhoosel C. *Nonlinear finite element analysis of solids and structures*. John Wiley & Sons; 2012.
- Chowdhury M, Nuruzzaman D, Kowser MA, MostafizurRahman M, Roy B, Chakraborty S, et al. Sliding friction of steel combinations. *Open Mech Eng J* 2014;8:364–9.
- Reddy J. *Mechanics of laminated composite plates and shells: theory and analysis*. CRC Press; 2004.